

Numerical investigation of the slipstream characteristics of a maglev train in a tunnel

Liu, Zhen; Zhou, Dan; Soper, David; Chen, Guang; Hemida, Hassan; Guo, Zijian; Li, Xianli

DOI:

[10.1177/09544097221100658](https://doi.org/10.1177/09544097221100658)

License:

None: All rights reserved

Document Version

Peer reviewed version

Citation for published version (Harvard):

Liu, Z, Zhou, D, Soper, D, Chen, G, Hemida, H, Guo, Z & Li, X 2022, 'Numerical investigation of the slipstream characteristics of a maglev train in a tunnel', *Proceedings of the Institution of Mechanical Engineers, Part F: Journal of Rail and Rapid Transit*. <https://doi.org/10.1177/09544097221100658>

[Link to publication on Research at Birmingham portal](#)

Publisher Rights Statement:

Liu Z, Zhou D, Soper D, et al. Numerical investigation of the slipstream characteristics of a maglev train in a tunnel. Proceedings of the Institution of Mechanical Engineers, Part F: Journal of Rail and Rapid Transit. May 2022. © IMechE 2022. doi:10.1177/09544097221100658

General rights

Unless a licence is specified above, all rights (including copyright and moral rights) in this document are retained by the authors and/or the copyright holders. The express permission of the copyright holder must be obtained for any use of this material other than for purposes permitted by law.

- Users may freely distribute the URL that is used to identify this publication.
- Users may download and/or print one copy of the publication from the University of Birmingham research portal for the purpose of private study or non-commercial research.
- User may use extracts from the document in line with the concept of 'fair dealing' under the Copyright, Designs and Patents Act 1988 (?)
- Users may not further distribute the material nor use it for the purposes of commercial gain.

Where a licence is displayed above, please note the terms and conditions of the licence govern your use of this document.

When citing, please reference the published version.

Take down policy

While the University of Birmingham exercises care and attention in making items available there are rare occasions when an item has been uploaded in error or has been deemed to be commercially or otherwise sensitive.

If you believe that this is the case for this document, please contact UBIRA@lists.bham.ac.uk providing details and we will remove access to the work immediately and investigate.

Numerical investigation of the slipstream characteristics of a maglev train in a tunnel

Zhen Liu², Dan Zhou^{1*}, David Soper², Guang Chen¹, Hassan Hemida², Zijian Guo², Xianli Li¹

Key Laboratory of Traffic Safety on Track of Ministry of Education, School of Traffic & Transportation Engineering,
Central South University, Changsha 410075, PR China

School of Civil Engineering, University of Birmingham, Birmingham, UK

ABSTRACT: High-speed maglev trains operate at higher speeds than conventional high-speed trains. This has implications on intensified aerodynamic issues, such as the transition between open air running and entering into a tunnel. In this paper, numerical simulation of a maglev train entering a tunnel is carried out using IDDES methods (based on SST k-omega model) to analyze the changing slipstream. The peaks and fluctuations of the slipstream are analyzed, together with the transient wake characteristics and TKE (turbulent kinetic energy) distributions. The influence of train nose length on the slipstream and its associated characteristics inside tunnels is also investigated in this paper. It was found that as the maglev train enters the tunnel, the wake slipstream at measuring points close to tunnel entrance increases significantly then decreases slightly with the increase of distance to tunnel entrance. Overall, the fluctuation and magnitude of slipstream inside tunnel is larger than that on open line, more specifically, the maximum TKE generated inside tunnel is 7.62% larger than that on the open line at contour $X=3H$ behind the train tail. Besides it takes longer time for the slipstream inside tunnel to return to the initial condition. These phenomena could be explained by that the scale of vortex structure formed behind the train tail is larger, the developing distance of the wake vortices in the streamwise direction is longer and the TKE generated is more significant inside tunnel. It was also found that increasing the nose length could effectively decrease the spatial scale and TKE of the wake vortices, which resulted on reducing the peak and pulsation of wake slipstream. Comparing to that of 5.4m, the peak of the wake slipstream of the maglev trains with the 7.4m and 9.4m nose lengths at $Y = 0.235m(0.385)$ is reduced by approximately 23.7%(58%) and 35.9%(82.2%) on open field, and by about 3.6%(4.7%) and 14%(18.5%) inside tunnel. Besides, the maximum TKE at contour $X=2H/3H/5H$ behind the train tail decreases about 14.4%/10.7%/11.3% and 51%/31.5%/18% as the nose length increase to 7.4m and 9.4m respectively.

1 Introduction

Compared with conventional high-speed trains, the maglev train completely eliminates the adverse

*Corresponding author: Dan Zhou

E-mail address: zd_lzj@126.com

32 effects caused by wheel-rail contact, which greatly raises the opportunity for higher operating speeds.
33 In recent years, research on maglev systems have been carried out mainly in China, Japan, Germany,
34 USA and other countries, with a view to trial operation lines under construction or recently opened.
35 Due to the environmental limitations and the requirement to achieve the desired operation speed, it
36 typically required that up to 50% of a journey to be within a tunnel. ¹For example, the central
37 Shinkansen project in Japan, started in 2013, includes a tunnel length of 24.6km, and the total
38 proportion of the line in a tunnel totals 86%. However, it is known that train aerodynamic problems
39 are intensified in tunnel, due to the relative confinement, including the increasing slipstream
40 magnitude that could cause damage to tunnel infrastructures and danger to trackside workers.
41 Train slipstream are formed by the movement of a train through the air as the surrounding flow
42 moves with the train due to viscosity. ^{2,3}According to previous research, the slipstream of a high
43 speed train (HST) operating on open line has a typical profile including a nose region (upstream and
44 nose region), boundary-layer region and wake region (near-wake and far-wake region).^{4,5,6} The near-
45 wake region is dominated by an unsteady gust peak created by a pair of counter-rotating vortices,
46 which brings the major adverse effect and receives special attention from researchers. A great
47 number of experiments and numerical simulations has been done to investigate the characteristics
48 of the vortex street (frequency, length scale, motion, etc.) and slipstream profile of HST, passenger
49 train and freight trains operating on open field.^{3,7,8,9,10,11,12} Results indicated that the characteristic
50 large-scale vortex structure varies from train-to-train due to a sensitive to the shape of tail train, as
51 well as being influenced by the track as it extends.^{3,5,13} Besides, the instantaneous flow structure and
52 aerodynamic performance of high-speed trains under cross-wind are also been widely investigated
53 ^{14,15,16}. The influence of geometry of the train and objects around the train (e.g. train nose shapes,
54 shelters, windbreaks, air fences) on the distribution of velocity and the characteristics of the vortices
55 are further investigated^{17,18,19,20}. Maglev trains operate at high train speeds, with the track positioned
56 relatively high above the ground and there isn't any bogies which is different from other trains.
57 However, few investigation have been done to investigate the slipstream behaviour and vortices
58 generated by maglev trains.
59 The flow inside tunnels is more unsteady and turbulent than that around trains in open air.^{21,22} In
60 addition, the velocity around trains in tunnels increases due to the piston effect. Full-scaled
61 experiments and moving model rig tests (MMR) have been carried out to assess the slipstream
62 development of a HST in a tunnel or confined space.^{23,24} Results indicated that the gust peak is
63 proportional to operating speed and related to train and tunnel length, shape of train end and
64 blockage ratio. It has also been noted that it takes a longer time for the air inside a tunnel to return
65 to initial condition comparing to that on open line. CFD simulations have also been carried out,
66 mainly using RANS (Reynolds-averaged Navier-Stokes) methods due to the large computational
67 resource required to simulate a moving train.^{25,26,27,28} However, URANS has its limitations to
68 measure highly turbulent slipstreams quantitatively since it fails to predict the developing of vortices
69 and the correlated dynamic response,²⁹ which the DES or LES methods are capable of doing. With

70 the development of computational capability, Khayrullina³⁰ simulated trains passing through a
71 platform using LES method. The wind conditions when the train enter and exit the platform is
72 analysed to assess its hazard to objects and passengers on the platform. Though these researches
73 show that the slipstream yields a much larger magnitude peak value in a tunnel, little is known for
74 the fundamentals of its formation and whether the assessment for slipstream in open field³¹ is
75 suitable for that in confined spaces^{24,25}.

76 Since the wake flow structures formed by the separation of boundary layer at train tail have
77 significant impact on wake gust, efforts have been made to reduce the adverse effect of the
78 slipstream by optimizing the train nose shape. The results of Bell, et al¹³ showed that the angle of
79 the roof influences the separation of the tail train surface and further induces vortices of different
80 dominating frequencies and length scale. As a result, a shorter nose leads to thicker boundary layer
81 at train tail, higher slipstream peak and more vortex structures in the wake.^{2,32,33,34} More specifically,
82 Chen² and Li³⁴ investigated the effect of nose length on slipstream development quantitatively by
83 comparing the “characteristic velocity” defined by Technical Specifications for Interoperability
84 (TSI)³¹, and the peak and averaged slipstream at the TSI trackside and platform position. Results
85 show that the effect on increasing nose length to reduce slipstream peak is significant in particular
86 at trackside position. However, the influence of nose length on slipstream in tunnel is still ambiguous.
87 In this paper, the slipstream induced by a maglev train entering tunnel is investigated and simulated
88 using the IDDES numerical model. This method is adopted to capture the transient turbulence
89 characteristic and to understand the mechanism of the changing on slipstream near the tunnel portal
90 and inside tunnel. Firstly, the grid independence validation is done to choose an appropriate mesh
91 and the numerical model is validated by comparing the history curve of velocity and pressure with
92 that obtained from a full-scale experiment. Then the slipstream velocity at measuring points along
93 the tunnel is discussed in section 3.1. The magnitude and fluctuation of slipstream are analysed
94 through the changes on instantaneous wake structure and turbulent kinetic energy (TKE)
95 distribution. Section 3.2 further investigate the effects of nose lengths on wake slipstream and
96 vortices inside the tunnel. The result obtained in this paper help to develop an understanding of the
97 slipstream variations in tunnel and could present a reference on assessing transient slipstream
98 velocity gusts in tunnels.

99 **2. Numerical simulation**

100 **2.1 Computational method**

101 The flow field is highly unsteady when a high-speed maglev train enters a tunnel, and the air inside
102 the tunnel is severely compressed and its state changes over time. Considering the expression for
103 Reynolds number: $Re = \frac{ul}{\nu}$, taking the train height H as feature length, which is 0.3m, the Reynolds
104 number of the flow field around the maglev train in this study is $\sim 2.38 \times 10^6$. This number is much

105 higher than 2.5×10^5 , which is the critical Re for the flow around trains³¹. Therefore, overall, the
 106 solver to simulate the flow of this case is viscous, three-dimensional, compressible, unsteady and
 107 turbulent.

108 Some researchers solved the flow field around the train in open line using Lattice Boltzmann
 109 Method, which is mesh free and had its advantage on parallel computing^{15,16,35}. Apart from this,
 110 most of researchers calculate the flow field around the train by numerically solving the N-S
 111 equations (LES, RANS). To simulate a train passing through a tunnel requires large computational
 112 resource, thus almost all studies of this problem were conducted using RANS (Reynolds-averaged
 113 Naiver-Stokes) methods. However, RANS has its shortage in that the fluctuated terms are averaged
 114 and therefore the transient characteristics of the flow and vortices cannot be observed. LES (Large-
 115 eddy simulation) is induced to simulate the instantaneous flow of train operating on open line, but
 116 the required mesh number and computational resources is still too much for simulation of moving
 117 trains. In contrast, the DES (Detached-eddy simulation) method combines the advantages of LES
 118 and RANS, to enable the transient development of large-scale vortex structures to be captured within
 119 acceptable computational resource. A drawback of this method is that the accuracy of traditional
 120 DES methods are very sensitive to grid quality and density near the wall, and may cause log-layer
 121 mismatch and grid-induced separation where the boundary layer is relatively thick and the
 122 separation region is small. As this study considers the complex interaction of the flow within
 123 changing infrastructure geometries, the IDDES model is adopted, based on the k-omega SST model
 124 to simulate the near wall region. This model has been widely adopted by previous researches to
 125 predict aerodynamic slipstream development.^{2,32,34,36} The governing equation of this k-omega SST
 126 model is:

$$127 \quad \frac{\partial k}{\partial t} + \frac{\partial}{\partial x_j} (k \bar{u}_j) = \frac{\partial}{\partial x_j} \left[\left(\nu + \frac{\nu_t}{\sigma_k} \right) \frac{\partial k}{\partial x_j} \right] + P_k - \beta^* k \omega \quad (1)$$

$$128 \quad \frac{\partial \omega}{\partial t} + \frac{\partial}{\partial x_j} (\omega \bar{u}_j) = \frac{\partial}{\partial x_j} \left[\left(\nu + \frac{\nu_t}{\sigma_\omega} \right) \frac{\partial \omega}{\partial x_j} \right] + \alpha \frac{P_k}{\nu_t} - \beta \omega^2 + 2(1 - F_1) \sigma_\omega^2 \frac{1}{\omega} \frac{\partial k}{\partial x_i} \frac{\partial \omega}{\partial x_i} \quad (2)$$

$$129 \quad \nu_t = \frac{a_1 k}{\max(a_1 \omega, |S| F_2)} \quad (3)$$

130 F_1 and F_2 represent the SST blending functions. Detail of the equations could be found in Liu, et
 131 al.³⁷. In IDDES model, the sink term in equation(1) is solved as follows:

$$132 \quad \beta^* k \omega \rightarrow \frac{\rho k^{3/2}}{l_{HYBRID}}, \quad l_{HYBRID} = \tilde{f}_d (1 + f_e) l_{RANS} + (1 - \tilde{f}_d) l_{LES} \quad (4)$$

133 l_{HYBRID} is modified length scale to combine DDES with WMLES scales. Multiple length scales
 134 are introduced in this formula, where the length scale of RANS is defined as $l_{RANS} = \kappa^{1/2} / (C_\mu \omega)$
 135 and the length scale of LES is defined as $l_{LES} = C_{DES} \Delta_{IDDES}$. The elevating function $f_e =$
 136 $\max((f_{e1} - 1), 0) \psi f_{e2}$, aiming at preventing the excessive reduction of the RANS Reynolds
 137 stresses. The blending function $\tilde{f}_d = \max((1 - f_{dt}), f_B)$ and $f_{dt} = 1 - \tanh((8r_{dt})^3)$ where the
 138 empirical blending function $f_B = \min(2 \exp(-9\alpha^2), 1.0)$. By this way the length scale l_{HYBRID}
 139 is able to transfer between l_{WMLES} and \tilde{l}_{DDES} . Besides, in the IDDES model, the new grid length
 140 scale is calculated by the following formula:

141
$$\Delta_{IDDES} = \min(\max(0.15d, 0.15\Delta, \Delta_{min}), \Delta) \quad (5)$$

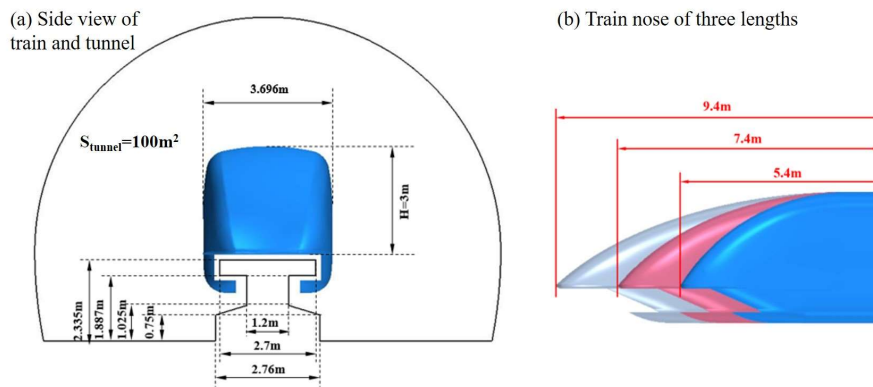
142 Where Δ_{min} is the minimum distance between the center of a grid cell and the center of an adjacent
 143 grid cell. Readers may find the complete formulations of the in IDDES model in Shur, et al.³⁸. The
 144 relevant control equations are solved using the CFD software STAR-CCM+ based on the finite
 145 volume method (FVM), and a SIMPLE pressure-velocity coupling method is also adopted. The
 146 second-order upwind scheme is used for the discretization of the convection and diffusion terms.
 147 The time derivative is discretized using the second-order implicit scheme for the unsteady
 148 calculation. The time step Δt is set as $4 \cdot 10^{-5}$ s, estimated by CFL (Courant–Friedrichs–Lewy) \leq
 149 1 ($CFL = \Delta t \cdot v / \Delta x_{min}$, where v is the train operating speed and Δx_{min} is 0.005m in this paper)^{36,30}.

150

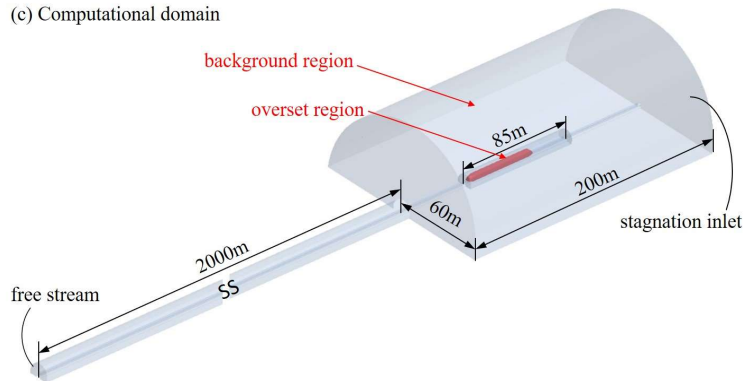
151 2.2 Model and computational domain

152 In order to obtain the information of the viscous boundary layer and control the total number of
 153 grids at the same time, a 1:10 reduction ratio in size is used for the maglev train and tunnel model.
 154 The shape and velocity of the maglev train model selected in this paper is based on the TR08 maglev
 155 train operating in Shanghai, with two carriages of a total length of 54.4m. The size of the train and
 156 track is given in **Figure 1(a)**. The width and height of the maglev train are referred as characteristic
 157 width (W) and height (H) in this paper. The original streamlined length of the train head is 5.4m and
 158 is stretched to 7.4m and 9.4m in the axial direction to study the influence of the nose length. The
 159 cross-sectional area of the single-tracked tunnel is 100m^2 and the length is 2000m.

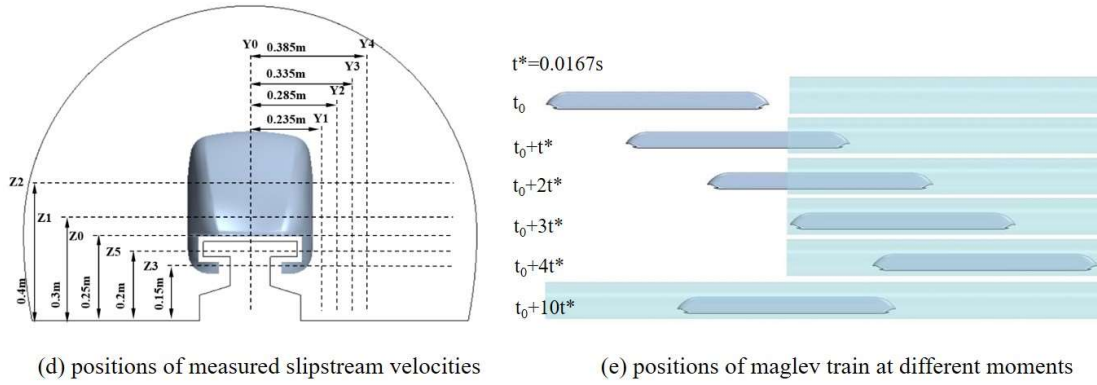
160



(c) Computational domain



161



162
163
164
165
166
167
168
169
170
171
172
173
174
175
176
177
178
179
180
181
182
183
184
185

Figure 1 Schematic diagram of the maglev train model and computational domain

An overset mesh is adopted over sliding mesh techniques to simulate the train's motion, since the continuous development of vortices through interface have strict requirement for the accurate information transfer between stationary and moving regions. Different from the sliding mesh method that uses a first-order area-based interpolation,³⁹ the overset mesh technique is considered as a high-order interface treatment and has been well-developed in the past decade to improve the accuracy and quality of the simulation at interface meshes⁴⁰. The whole computational domain of maglev train entering the tunnel is divided into two regions: overset region and background region, as shown in **Figure 1(c)**(note that dimensions are given as full-scale values). The maglev train is started 50m away from the tunnel entrance to ensure that the flow field around the train is well-developed before it enters the tunnel. The train tail is 100m away from the domain boundary, which is long enough to ensure that the contribution of dissipation of turbulence vortex to the flow around the train is negligible. To avoid overlapping, such as grid interpolation errors affecting the flow field information near the train and the wake region, the cross-sectional area of the overset region is 0.9 times the cross-sectional area of the tunnel and the distance of the train tail to the boundary of overset region is approximately 10H. The boundary settings are also given in **Figure 1(c)**. For the overset region, the grids used for interpolation calculation are overset boundary, and the surfaces of the train are set as a wall. For the background region, the end of the tunnel is given a free stream boundary, the back surface of open field is set as stagnation inlet, and the rest are set as wall. The distribution of measuring points of slipstream velocities is shown **Figure 1 (d)**. Besides, different time instants of the maglev train entering the tunnel are chosen as shown in **Figure 1 (e)** to analyse the change of slipstream and vortices, where t^* is the time required for the maglev train to travel 2m.

2.3 Mesh

187 The entire computational domain is divided by a trimmed cell mesh. Due to the fact that areas in
188 which flow separation and vorticity are usually generated in are mainly located at the head/ tail of
189 the train and the gap between the train and the track, a finer mesh is adopted in these regions. Coarse,
190 medium and fine meshes were built to verify the independence of the grid, as shown in **Figure 2(a)**.
191 The sizes of the first cells on the train surface are 0.007m, 0.005m and 0.004m, and 15, 25 and 30
192 prism layers are established on train surface with at total grid number of 17.6, 27.2 and 31.7 million

193 for the coarse, medium and fine meshes, respectively. The comparison of results from each mesh
 194 density for slipstream velocity at tunnel entrance is shown in **Figure 2(c)**. It can be seen that the
 195 results agree well with each other, while the coarse mesh tends to overpredict the velocity,
 196 particularly at the wake. The peak and profile of the slipstream predicted by medium mesh is very
 197 similar to that of the fine mesh, but there is some discrepancy in the wake region. It is understandable
 198 since there are a large number of vortices exist in wake region that could be captured using IDDES
 199 method, the flow there is highly unsteady and the velocity variation is related to both space and time.
 200 Therefore, it is inevitable that the transient velocity curve in the wake region cannot be the same at
 201 a specific moment and position. Similar conclusion could be seen in mesh validation in Khayrullina,
 202 et al.³⁰, in which utilises the LES method to simulate a train passing through a platform, and the
 203 velocity profile at wake region also deviates a lot between fine and medium mesh. Thus, medium
 204 mesh is adopted in this paper.

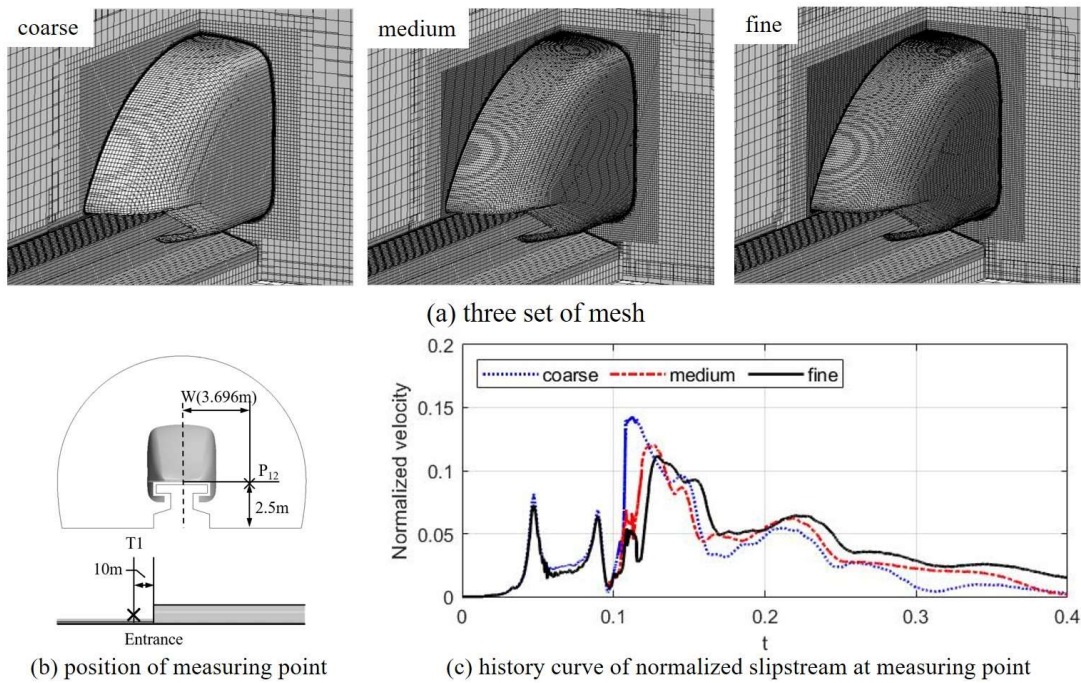


Figure 2 Result of mesh sensitivity

205
 206
 207 The specific diagram of the mesh at tunnel entrance, around train and track is shown in **Figure**
 208 **3(b)**. In order to better simulate the velocity distribution in the viscous flow region of the train, the
 209 first layer of the wall is estimated with a thickness of $y^+ \approx 5$, with 25 prism layers and a stretching
 210 ratio of 1.15. A coarser prism mesh is added on tunnel and track surface. The wall y^+ of train surface
 211 at $10t^*$ after the train entered the tunnel, as shown in **Figure 3**. It can be seen that y^+ for most of the
 212 mesh on train body is less than 3. To ensure high interpolation accuracy for overlapping grids and
 213 successful mesh assembly during train motion, the size of the acceptor cells in the overset region is
 214 similar to that of the donor cells in the background region. There are 0.02 m and 0.032 m for the
 215 acceptor and donor cells, respectively. The mesh for the overset and background region are coloured
 216 with blue and black in, with corresponding grid numbers of 16 and 11 million, respectively.

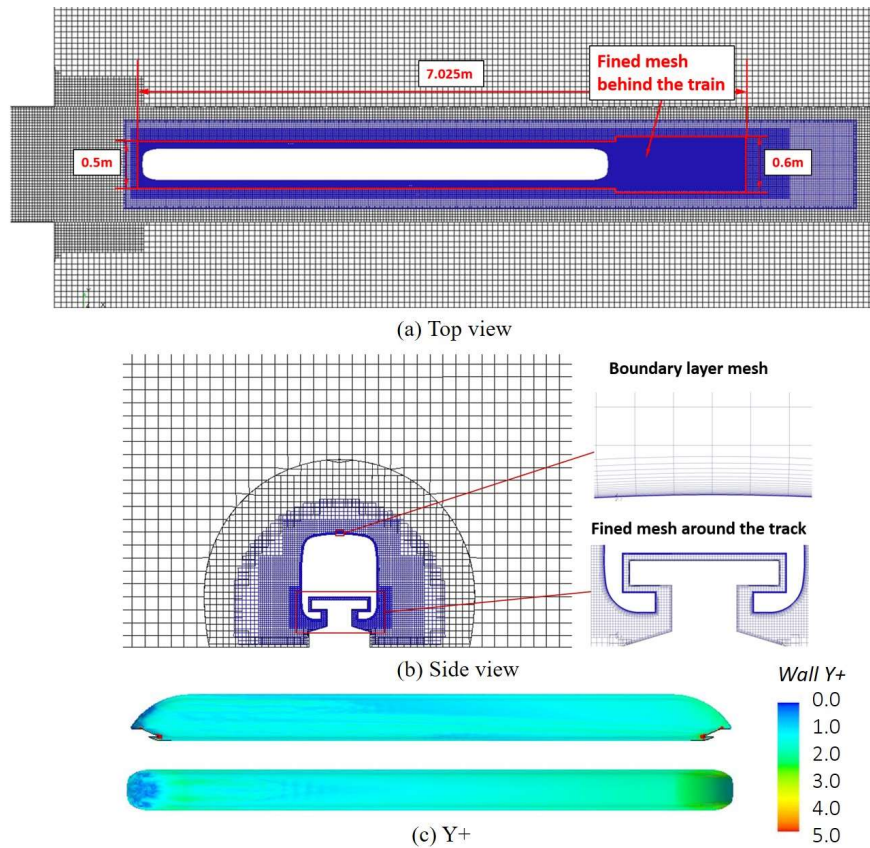


Figure 3 Computational mesh

2.4 Model verification

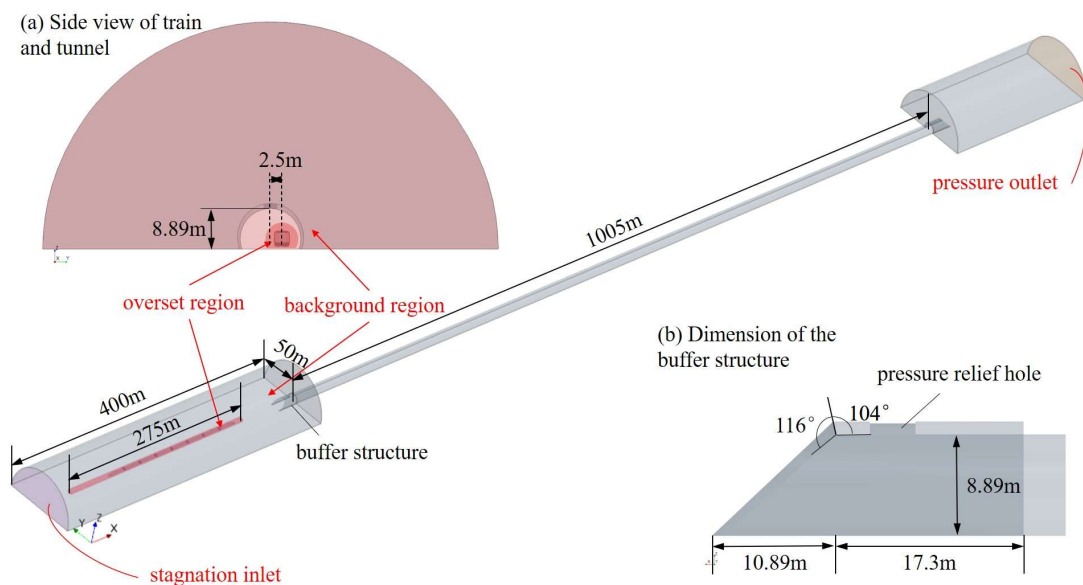
In order to verify the accuracy and the reliability of the numerical setup in this paper, the numerical simulation results of a CRH2C train passing through a tunnel at a speed of 300km/h are compared with the results obtained from a full-scale experiment. The test train is composed by eight cars with a total length of 201.4m and a running speed of 300km/h. The tunnel is a double-track tunnel with a total length of 1005m and a cross-sectional area of 100m². Besides, a buffer structure with pressure relief hole is constructed at tunnel entrance and exit. More details of the pressure and velocity monitor sensors and the setup of full-scale experiment are illustrated in Liu et al (2019)²⁵.

Based on the train and tunnel model of the full-scale experiment, the dimensions of the computational domain for the validation case is constructed as shown in **Figure 4**. A 1:10 reduction ratio in size is used for the CRH2C train and tunnel, which is the same as the reduction ratio for the maglev train in this paper. Similarly, the boundary conditions and the cross-sectional shape of the overset region are also determined following the setup adopted for the maglev train in this paper.

A trimmed cell mesh is adopted to divide the overset and background region as shown in **Figure 5**. Mesh around the train nose, the wake region and tunnel portal are refined with a size of 0.00625, which is a bit coarser comparing to the grid size adopted for the maglev train in this paper. This is due to the test train is composed by 8 cars, which will generate massive grid number if completely follow the grid size in this paper, leading to extremely high computational costs by using IDDES numerical model. The first layer of the wall is estimated by $y^+ \approx 5$ with a thickness of 0.01, with 13

238 prism layers and a stretching ratio of 1.5. The size of the acceptor cells in the overset region and the
 239 donor cells in the background region are both 0.025m. By this way, the total grid number for overset
 240 region and background region are 11.2 and 14.7 million respectively.

241 The slipstream and pressure history curve obtained from the simulation are compared with that from
 242 the full-scale experiment as shown in **Figure 6**. Due to the reduced scale of the simulation, time and
 243 pressure are non-dimensioned by L_{tr}/v_{train} and $0.5*\rho*v_{train}^2$ respectively for a better comparison. It
 244 could be seen in **Figure 6(a)** that in general the simulation result fits well with the experimental
 245 result on predicting the velocity peak induced by train nose and near wake region, with a relative
 246 error of 3.5% and 6.4%. However, the velocity distribution in the wake region doesn't match in a
 247 very good way, which is understandable since the instantaneous velocity obtained from one run is
 248 unsteady due to the highly turbulent flow, especially in the wake region. Besides, the velocity around
 249 the train body is a little underestimated by the simulation, this might due to the reduced-scale and
 250 the simplification on bogies potentially decreasing the effective blockage ratio. Overall, the
 251 prediction on the peak values and trend of the velocity are within acceptable error range. **Figure**
 252 **6(b)** shows the comparison of pressure coefficient on tunnel surface. The maximum positive and
 253 negative pressure coefficient obtained from the simulation are 0.3449 and -0.5633, and that from
 254 the experiment are 0.3505 and -0.5759, respectively. Therefore the relative error for the peak-to-
 255 peak pressure coefficient of tunnel train surface does not exceed 2%. The deviation between the
 256 simulation and full scale test at the second half section of time history curve of pressure on tunnel
 257 surface might due to the effect of environmental wind and certain error of actual running velocity
 258 during the experiment. In conclusion, the magnitude of slipstream and pressure wave could be
 259 satisfactorily predicted using the simulation settings in this paper.



260
 261

Figure 4 Computational domain for the validation case

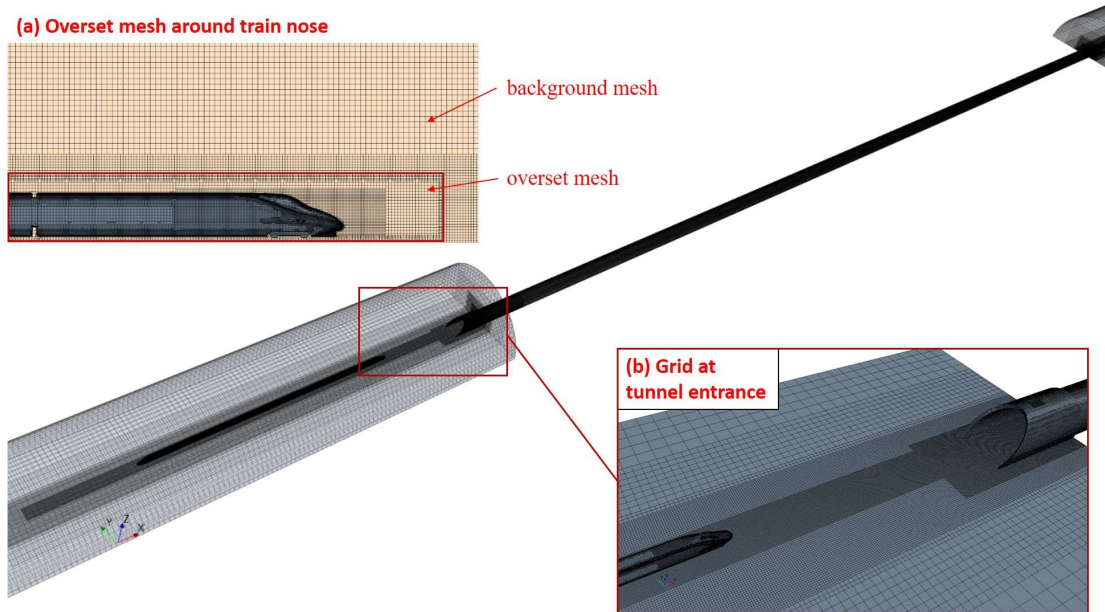


Figure 5 Computational mesh for validation case

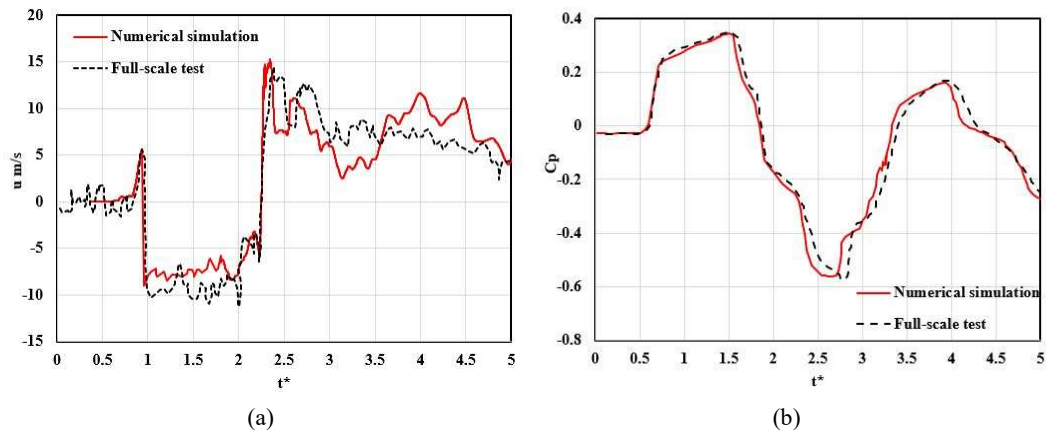


Figure 6 Comparison of full-scale test and numerical results (a) velocity variations (b) pressure variations

3 Numerical results

3.1 Reference case

3.1.1 Slipstream velocity

As referred to in the TSI and EN, horizontal velocity plays the vital role in the safety risk of instability for trackside workers and lineside equipment. Throughout this analysis the slipstream velocity is therefore defined by the horizontal velocity, and normalized by the train speed as below,

$$U = \frac{\sqrt{u^2 + v^2}}{v_{train}} \quad (1)$$

where u and v represent the streamwise and spanwise direction of the flow velocity, v_{train} is 119.4m/s.

The history curves of the normalized slipstream velocity at positions T1~T7 are shown in **Figure 7** (b)~(h), measured for 3 points at each position (P_{11} , P_{12} , P_{13}). The position of the 21 measuring

277 points relative to the train and tunnel is shown in **Figure 7(a)**. The red and blue dashed lines
278 represents the nose and tail of the train, and red and blue arrow represents the compression wave
279 and expansion wave, generated when train head and tail enters the tunnel separately.

280 The profile of slipstream at measuring points inside tunnel is affected by both the expansion and
281 compression pressure waves and the passing train. The influence of the pressure waves could be
282 concluded, from **Figure 7(d)~(e)**, to increase slipstream velocity magnitudes where the compression
283 wave passes and decrease the slipstream magnitude when the compression wave passes. The
284 influence of the passing train on the slipstream in tunnel is analysed based on the flow regions
285 proposed in Baker^{7,41,42}: nose region around the front of the train, boundary-layer region along the
286 length of train, wake region (near-wake and far-wake region) behind the train. For measuring
287 position P₁₂, the height at which is the same as the track upper surface, the slipstream shows a
288 significantly larger wake velocity among P₁₁~P₁₃. At T1 outside the tunnel entrance, a peak occurs
289 at nose region and tail of boundary region, with a more significant peak is observed at “near wake
290 region”. This is consistent with findings from previous research for a train running on the open line.
291 When the train passes T2, the slipstream velocity at “boundary layer region” and “near wake region”
292 increases due to the piston effect. As the distance from the measurement point to the tunnel entrance
293 increases (from T3 to T5), the velocity at nose and boundary regions gradually increases, while the
294 peak at the wake increases to its maximum at T4 then decreases. To be more specific, the velocity
295 at the rear of boundary layer region reaches the maximum soon after it enters the tunnel, then the
296 velocity at the body and head of boundary layer region reaches the maximum gradually, at
297 approximately 100m inside the tunnel. The profile and maximum peak magnitude of slipstream in
298 each region at measuring points T5, T6 and T7 shows slight difference. This could be due to the
299 position of the measurement points far from the tunnel entrance, therefore the velocity of the wake
300 is almost no longer affected by the train entering the tunnel.

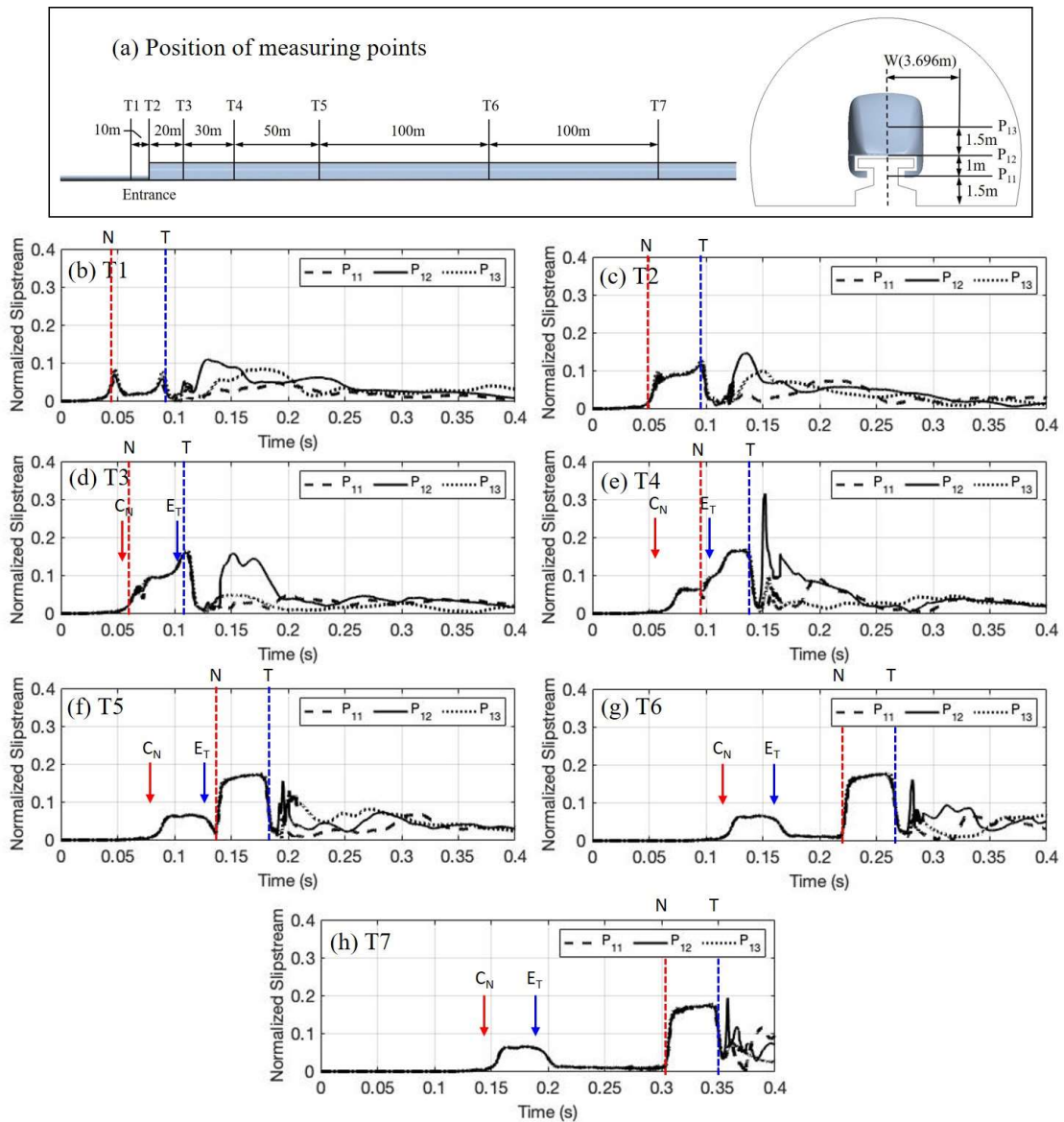
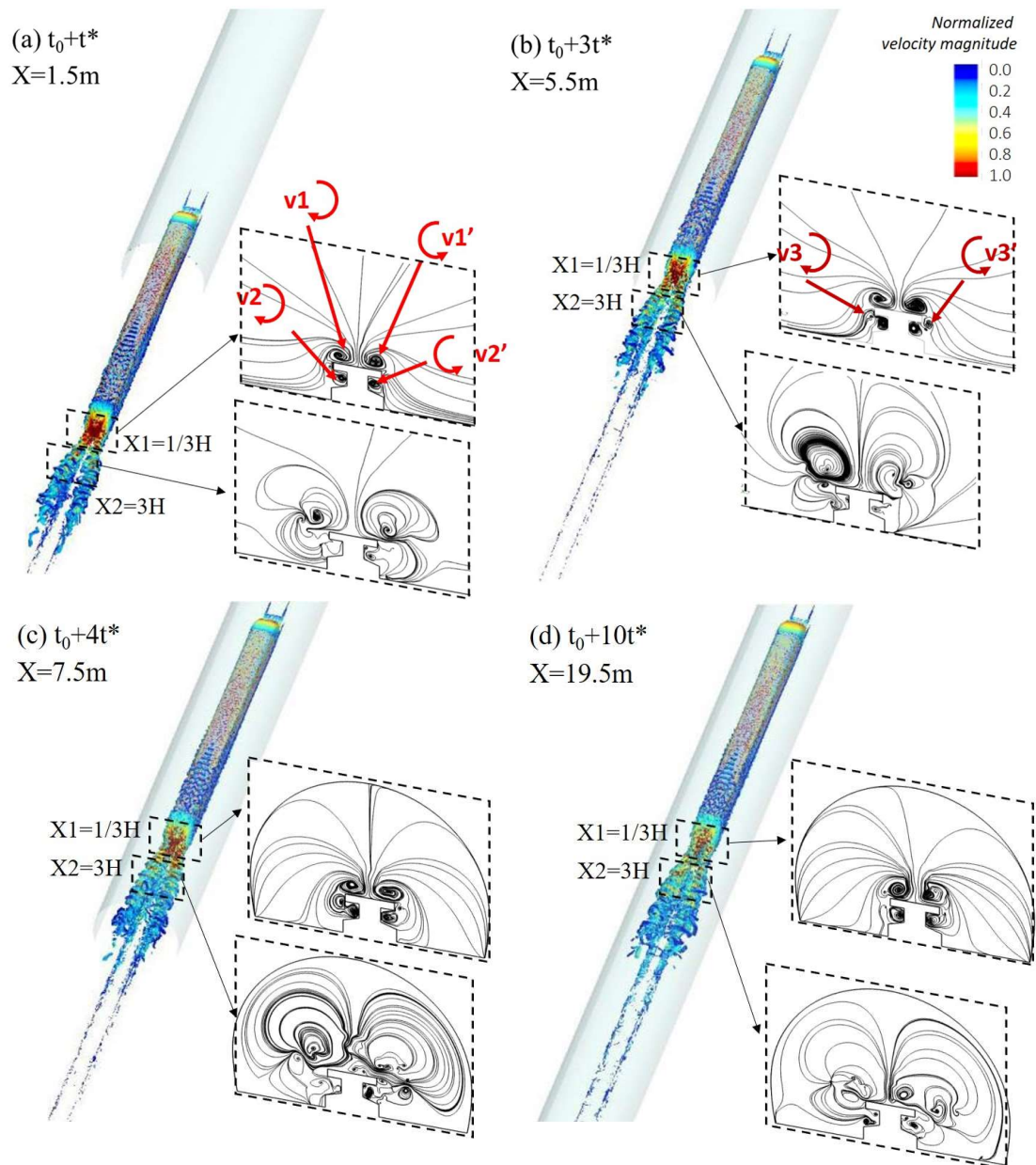


Figure 7 Time history curve of slipstream velocity

3.1.2 Wake vortex structure

Slipstream velocity is closely related to the distribution and strength of wake vortex. To understand the change of velocity as the train enters into the tunnel, the instantaneous vortices generated around the maglev train, identified by Q iso-surface, are shown in **Figure 8**. The contours of the particle movements at $X1=1/3H$ and $X2=3H$ are given to analyse the development of the instantaneous vortices.



309

310

311 **Figure 8** Q iso-surface at different moments of maglev train enters the tunnel ($Q=100000$) (X : the distance from
312 the head of the train to tunnel entrance)

313 As the air accelerates and flows downward at the tail of the train, the backpressure gradient and the
314 momentum loss in the boundary layer increases. It forces the boundary layer to separate, forming a
315 pair of large-scale symmetrical vortices (v_1 and v_1'), which can be seen clearly in **Figure 8(a)** when
316 the train tail is far away from the tunnel entrance. This pair of coherent structures is the most
317 significant one in the wake region of a maglev train, and its formation mechanism is similar to that
318 of a high-speed train. Since the track of a maglev train is different from that of the high-speed train,
319 there is another pair of smaller vortices (v_2 and v_2') beneath the maglev track. Besides, this two
320 pair of vortices show good symmetry with a clear shape when they just formed at contour $X_1 = 1/3H$
321 behind the train tail due to the simple geometry of the maglev train. It is worth pointing out that
322 normally the instantaneous flow field at near wake region of a high-speed train is much more dis-
323 ordered since the bogies and windshield generate large amount of turbulence that finally goes into

324 the wake^{2,8,34}. The vortices generated by the maglev train gradually develops as the distance from
325 the rear of the increases. At the contour farther from the tail of the train ($X=3H$), these pair of large-
326 scale vortices split into weaker and small-scale coherent structures. Besides, the velocity in the near
327 wake region decreases with the vortices shedding backwards, and the velocity magnitude near the
328 vortex core is larger than that at the outer edge of the vortex. At t_0+3t^* , the rear of the train has just
329 entered the tunnel entrance. Due to the blockage effect, the velocity sweeping downwards at the rear
330 of the train increases, leading to a spanwise moving tendency of the vortex structure close to the
331 rear of train. Also, a small pair of vortices (v_3 and v_3') formed as the air flow over the side of train
332 surface and interact with the side of the upper track, which could be seen at contour $X_1=1/3H$. The
333 small-scale vortex v_3 will split as it develops, with part of it involving in the large-scale vortices v_1 ,
334 and the rest spreading downward and spanwise. At t_0+4t^* when the train tail is about 2m inside
335 tunnel, the distribution of the vortex is significantly wider and the vortex length scale enlarges. The
336 wake structure becomes disordered at the tunnel entrance due to the turbulent airflow. However, the
337 size of tail vortex continues to grow inside the tunnel as it is shedding backwards towards the
338 entrance, thus increasing the length of the development, as could be seen when the train head is
339 19.5m inside tunnel at t_0+10t^* . Compared the contour at $X=3H$ with that in **Figure 8(a)**, it could be
340 clearly seen that many small vortices generate and the air flow at the wake is more disordered when
341 the wake is inside tunnel. The scale of the vortex inside the tunnel significantly enlarges and the
342 distance between the two vortices narrows. Due to the acceleration of the air flow inside tunnel, an
343 earlier separation occurs at the rear of the train so that the position where the vortex fall off moves
344 upward, which could be seen by comparing the position of the vortex at contour $X=1/3H$ in **Figure**
345 **8(a)** and (d). Besides, due to the larger negative pressure in the wake region, the suction effect on
346 the wake vortices is enhanced so that the distance between the pair of vortices is narrowed. The
347 spatial scale of the vortices in the tunnel significantly increases with the increasing velocity
348 sweeping downward, which also explains why a relatively larger wake velocity exists on the
349 trackside inside the tunnel.

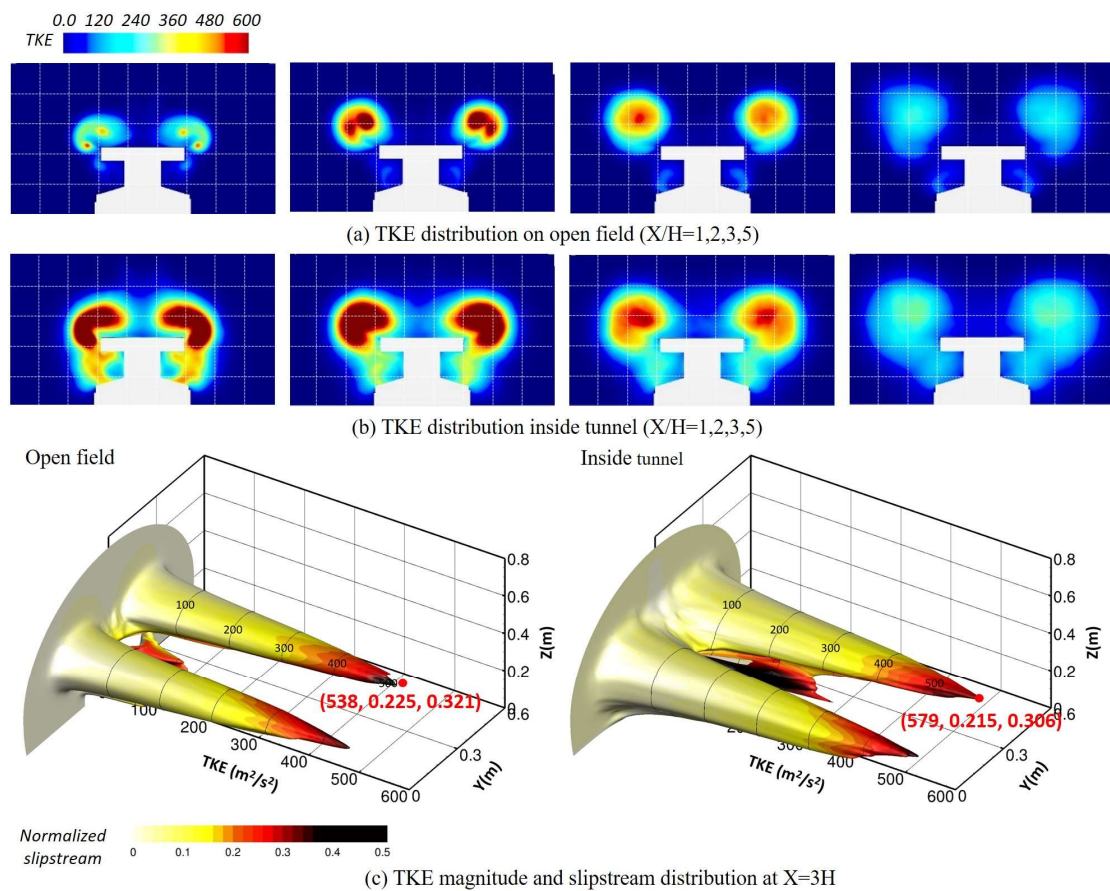
350 *3.1.3 Turbulence intensity*

351 TKE is a quantity to measure turbulence quantitatively, and has been used to analyse the wake of wind
352 turbines, buildings and trains under crosswind (Influence of atmospheric stability on wind-turbine
353 wakes: A large-eddy simulation study, 2015; Atmospheric turbulence effects on wind-turbine wakes:
354 An LES stud, 2012; Numerical calculation of the slipstream generated by a CRH2 high-speed train,
355 2016; Dynamic analysis of the effect of nose length on train aerodynamic performance, 2019). In
356 this paper, turbulent kinetic energy (TKE) is introduced to measure the fluctuation and the overall
357 level of turbulence in the wake. It is calculated by summing the squared fluctuating velocity of the
358 three axial directions,

$$359 \quad \text{TKE} = \frac{1}{2} (\overline{u'^2} + \overline{v'^2} + \overline{w'^2}) \quad (2)$$

360 u' , v' and w' are fluctuating velocities on x, y, z direction, which are the difference between the

361 instantaneous velocity and the average velocity. The instantaneous and average velocity adopted are
 362 monitored from t_0+5t^* to t_0+20t^* . **Figure 9(a)(b)** compares the TKE distribution in near wake region
 363 when maglev train runs on open field and inside the tunnel. The positions of the contours are 1H,
 364 2H, 3H, 5H from the tail of the train respectively and the area of the white dashed-line square is
 365 1m^2 .
 366 TKE is mainly generated above and on both sides of the maglev track, where the wake vortices
 367 distribute. Therefore, it also reflects clearly the change in the scale of the vortex and the trace of the
 368 vortex shedding spanwise and upwards. The magnitude of TKE increases near the tail of the train,
 369 and gradually decreases as the distance increases. When the maglev train operates inside the tunnel,
 370 the distribution range and the magnitude is significantly larger. This is due to the larger streamwise
 371 velocity inside tunnel and the interaction of the airflow and the track, which causes a stronger
 372 velocity fluctuation in the wake. The increase in distribution range is consistent with the conclusion
 373 that the spatial scale of the wake vortex in the tunnel is larger than that on the open line. It is worth
 374 noting that the distribution of the vortex inside tunnel ranges mainly between 2m~4m above the
 375 ground, and 0.5m~3.5m from the centre of the train (COT). It explains the relatively low velocity
 376 peak in the wake at measuring points at $Y=0.369\text{m}$ (section 3.1.1).



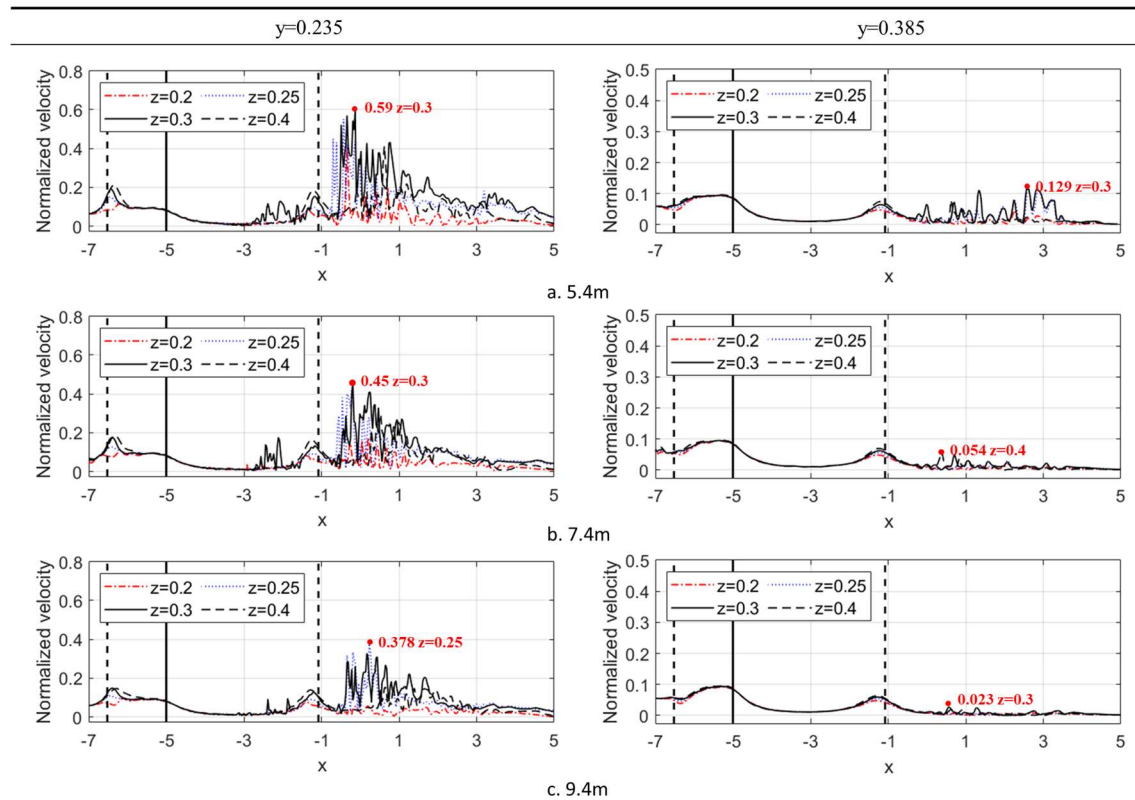
377
 378 **Figure 9** Distribution of TKE at contours behind the train ($X/H=1,2,3,5$)
 379 To quantitatively compare the TKE generation before and after maglev train entering the tunnel, the
 380 magnitude of TKE at contour $X=3H$ is shown in **Figure 9(c)**, and is coloured by normalized
 381 slipstream. The maximum slipstream near vortex v1 doesn't show much difference, however the

382 maximum velocity and TKE near vortex v2 is much larger inside tunnel. The position and magnitude
 383 where maximum TKE generates are marked in the figure. It could be seen that at this contour, the
 384 maximum TKE generated inside tunnel is 7.62% larger than that on the open line. Besides, both y
 385 and z coordinates inside tunnel are smaller than those on the open line. It indicates that the flow
 386 development of wake vortex is constrained by the tunnel wall, leading to the position of vortex core
 387 slightly closer to the track and COT.

388 3.2 The effect of nose length

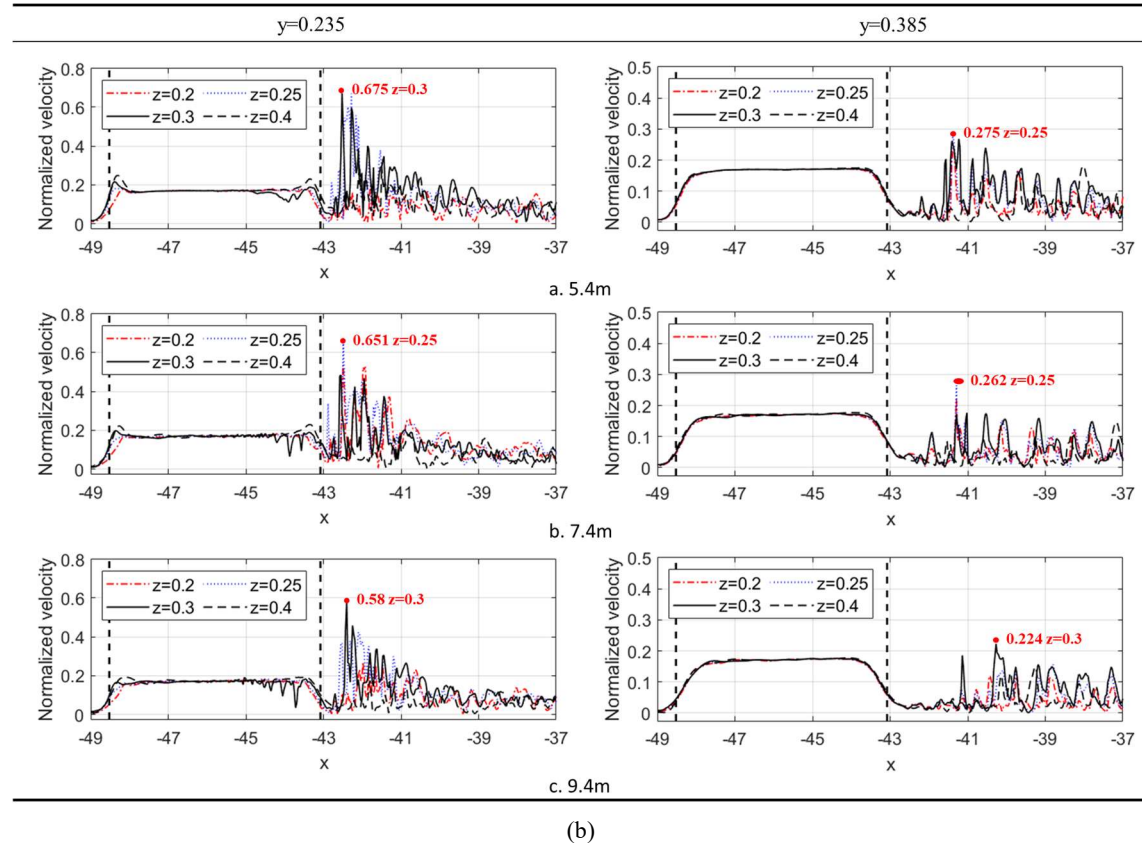
389 3.2.1 Slipstream velocity

390 As we discussed in 3.1.2, the maximum slipstream velocity is expected to occur from $Z=0.2$ to
 391 $Z=0.3$ where the main wake vortices generate. Therefore, the measuring points are located at $Z=0.2$,
 392 0.25, 0.3 and 0.4 m to try to capture the maximum slipstream velocity when y (the distance from
 393 measuring point to central line) is constant. The spatial distribution of normalized slipstream along
 394 the streamwise direction of the maglev train before and after train tail enters the tunnel (t_0+t^* and
 395 t_0+10t^*) is shown as **Figure 10**. The position of the measuring points relative to the train and the
 396 location of the train at different time are shown in **Figure 1**(d)(e) respectively. The range of x-axis
 397 of the measuring lines are from 1m ahead the train nose to 6m behind the train tail. The two vertical
 398 dash lines in **Figure 10** represent the position of train head and tail, and the bold line is the position
 399 of the tunnel entrance. The peak value and the position where it appears are marked red in the figure.



400
 401

(a)



402

403

404

405

406

407

408

409

410

411

412

413

414

415

416

417

418

419

420

421

422

Figure 10 Spatial distribution of normalized slipstream for maglev trains of three nose lengths at different positions (a) $t_0 + t^*$ before the train tail enters the tunnel (b) $t_0 + 10t^*$ after the train tail enters the tunnel

The maximum slipstream velocity occurs at 0.25m~0.3m above the ground for maglev train of three nose lengths. After the maglev train enters the tunnel, relatively larger wake slipstream and fluctuation amplitude still exists at the position $20H$ from the rear of the train and $0.96W$ from COT. The slipstream in the annulus space between the train body and tunnel is basically unchanged when the nose length increases from 5.4m to 9.4m, but the reduction of the peak of the wake slipstream velocity and the reduce rate on its lateral and vertical direction is significant. Before the maglev train enters the tunnel, the peak of wake slipstream of the maglev trains with nose lengths of 7.4m and 9.4m is reduced by approximately 23.7%(58%) and 35.9%(82.2%) at 0.235m(0.385) from COT, compared to that of maglev with nose length of 5.4m. When the train is operating in the tunnel at $t+10t^*$, the increase of wake slipstream of the maglev train with a longer nose length is more notable. The peak of the wake slipstream of the maglev trains with the 7.4m and 9.4m nose lengths at $Y = 0.235m(0.385)$ is reduced by about 3.6%(4.7%) and 14%(18.5%), respectively. It can be concluded that the effect of increasing the nose length to reduce the wake slipstream peak velocity magnitudes is weakened inside the tunnel. To understand the difference on slipstream between three nose lengths, the flow pattern and wake structure are further analysed in the following sections.

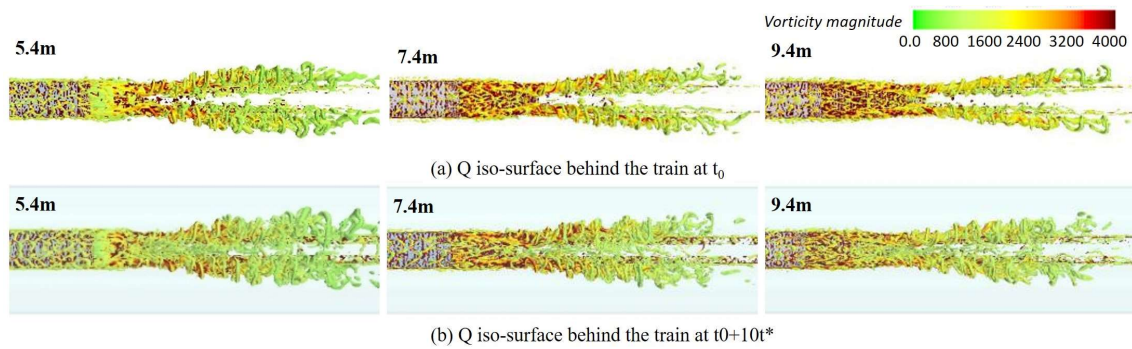
3.2.2 Wake vortices structure

423

424

Figure 11 considers the influence of the nose length on the wake vortex structure when the maglev train operates on open line and inside tunnel. The vortices are identified by Q criteria and coloured

425 with vorticity.



426

Figure 11 Q iso-surface at the wake of maglev train with different nose lengths ($Q=100000$)

427

428

The pair of large scale vortices induced by the separation at train tail are clearly identified in **Figure**

429

11. Comparing the vortex structure on open line to that inside the tunnel, it could be seen the wake

430

of the train with three different nose lengths exhibits a similar behaviour, that is, the vortices are

431

notably wider along with much more small-scale vortices generated when inside the tunnel. This is

432

due to the relative speed between the train and the surrounding air increases inside the tunnel, and

433

the mixing effect created by the confined space is strengthened. Besides, The tail of the train is

434

covered by high vorticity, indicating a strong circulation region. Vorticity is higher where closer to

435

the core of the vortex, and gradually weakens as the wake vortices shedding spanwise and

436

backwards. As the nose becomes longer, the scale of separation for the pair of vortices at the rear of

437

the train is thinner and the angle between the vortices becomes narrower. It is hypothesised that this

438

is due to the longer train nose decreasing the negative pressure behind the train tail, reducing the

439

suction and delaying the separation at the tail of the train. Besides since the velocity peak exists

440

where close to the core of vortexes, the thinner and narrower vortices generated by longer train nose

441

explains the smaller slipstream. Comparing to **Figure 11(a)** and **(b)**, this phenomenon is more

442

significant before the train enters the tunnel, which explains why the effect of nose length on

443

reducing wake velocity is less obvious inside tunnel. The small-scale vortices generated by the

444

maglev train entering the tunnel become less with increased nose length, and the vortex complexity

445

is therefore reduced. The magnitude of TKE in the wake is given in the next chapter to quantitatively

446

compare the wake unsteadiness inside the tunnel induced by different nose length.

447

448 *3.2.3 Turbulence intensity*

449

In order to measure the influence of nose length on the fluctuation of the wake inside tunnel, the

450

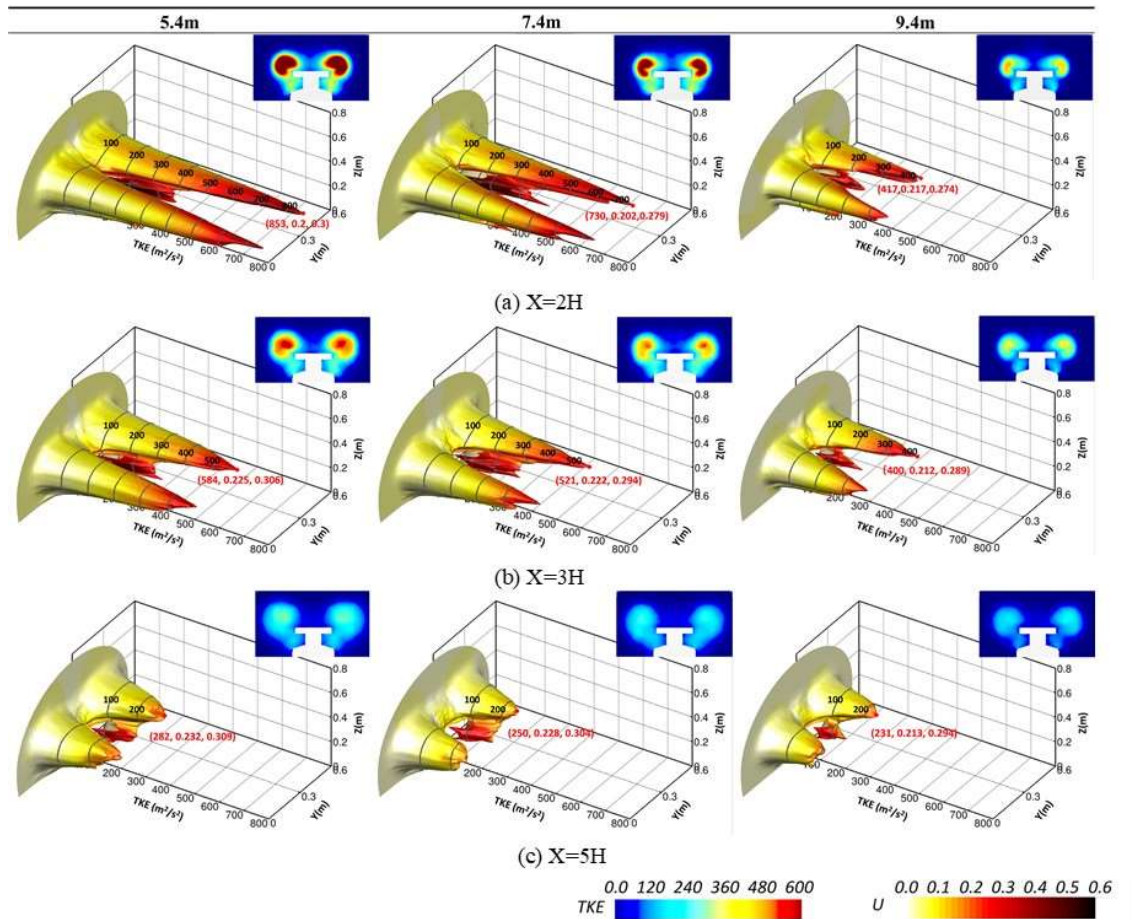
magnitude of TKE of different nose length inside tunnel at contours $X=2H/3H/5H$ behind the train

451

are shown in **Figure 12**. The detail of how TKE in tunnel is calculated and averaged is illustrated in

452

3.1.3.



453

454 **Figure 12** TKE and slipstream distribution of different nose length inside tunnel at contours behind the train
 455 (X/H=2,3,5)

456 As the distance from the train tail increases, the main TKE distribution area moves upward and
 457 sideward as the vertical movement and extension of the wake vortices. The magnitude and
 458 distribution area of TKE significantly decreases as the length of the train nose increases, and this
 459 phenomenon is particularly obvious in regions closer to train tail and for the case with nose length
 460 of 9.4m. This phenomenon is mainly related to the longer train nose delaying the separation of the
 461 boundary layer at the rear of the train, which leads to a significant reduction in the speed fluctuation
 462 in the three directions, further result in the reduction of the TKE. Comparing to that of 5.4m, the
 463 maximum TKE at contour X=2H/3H/5H decreases about 14.4%/10.7%/11.3% and 51%/31.5%/18%
 464 as the nose length increase to 7.4m and 9.4m respectively. It illustrates quantitatively the reduction of
 465 the fluctuation of slipstream velocity with the increase in nose length, and is consistent with the
 466 conclusion that vortex structures are thinner as nose length increases. The magnitude y and z axis
 467 where the maximum TKE generates inside tunnel is marked in the figure, also indicating how the
 468 position of the vortex core changes with the length of train nose. Considering the height of the track
 469 is 0.2335m, it could be seen that comparing to the that of 5.4m, the magnitude of where the
 470 maximum TKE generates above the track at X=2H decreases about 31.6%/39% as the nose length
 471 increases to 7.4m/9.4m. It is also noticed that the location of vortex core is closer to COT at contour
 472 X=2H when the train nose is shorter, and farther from the COT as the vortices developing away

473 from the tail of the train(contour $X=3H/5H$). This might due to the larger negative pressure region
474 generated by the shorter train nose at the rear of the train suctioning the flow to the COT. In the
475 meantime the scale of the pair of counter-rotating vortices generated by shorter train nose is larger,
476 and therefore moves further away from each other in spanwise direction as they shedding backwards.
477 In general, the location is about 0.5~0.7 m above the track and 2.1~2.2 m to the COT, which matches
478 the area where the peak of slipstream exists. However, though the area where high slipstream
479 distributes significantly decreases with the increase of nose length, the maximum slipstream doesn't
480 show much difference among three nose length.

481 **4 Conclusion**

482 Due to the special track structure of the maglev train and its simplification on bogies compared to
483 high speed train, the slipstream variation and development of wake vortex structure are different
484 from that generated by high speed trains. For the first time the process of a maglev train entering a
485 tunnel is simulated using the overset mesh method through an IDDES numerical simulation. The
486 vortex structures and TKE distributions change as the maglev train operates from open line to a
487 tunnel are discussed in detail, combining with its relationship with the magnitude and fluctuation of
488 the slipstream velocity. Besides, an approach to calculate the TKE inside tunnel is proposed,
489 enabling to quantitatively analyse and compare the effect of confined space on the fluctuation of
490 slipstream and the turbulence level of the wake. The effect of three nose lengths are further
491 investigated. A series of important conclusions can be drawn as follows:

492 (a) The magnitude and fluctuation of the slipstream inside tunnel are significantly higher than that
493 in open line. As the distance of measured points closed to the tunnel entrance increases, the
494 slipstream velocity at the rear of boundary region and wake region increases first, then the velocity
495 at the head of boundary region increases gradually. As the distance further increases, the slipstream
496 at "boundary layer region" keeps constant at its maximum, while that at the "near wake region"
497 decreases slightly then remains basically unchanged.

498 (b) As the train enters the tunnel, the velocity sweeping downwards at the rear of the train increases,
499 leading to a spanwise moving tendency of the vortex structure close to the rear of train. The spatial
500 scale of the tail vortex increases significantly and the distance between the vortices becomes wider,
501 explaining the larger velocity exits inside tunnel at the same position relative to the train.

502 (c) The magnitude of TKE near the train tail increases rapidly then gradually decreases as the
503 distance to train tail becomes longer. When operating inside a tunnel, the maximum TKE at $X=3H$
504 is 7.62% larger than that on the open line, indicating the larger velocity fluctuation inside tunnel.

505 (d) With increasing nose length, the spatial scale and complexity of the tail vortices decreases, and
506 the distance between the two flow direction vortices becomes narrower. This effect is more obvious
507 when compared to results from an open line. Comparing to the nose length of 5.4m, the z position
508 (above the track) of vortex core inside the tunnel at contour $X=2H$ decreases about 31.6%/39% as

509 the nose length increases to 7.4m/9.4m.
510 (e)The location where the maximum TKE is generated is similar among the three noses, which is
511 about 0.5~0.7 m above the track and 2.1~2.2 m to the COT, but the value and distribution area of
512 TKE inside tunnel are both significantly reduced. Comparing to that of 5.4m, the maximum TKE at
513 contour $X=2H/3H/5H$ behind the train tail decreases about 14.4%/10.7%/11.3% and 51%/31.5%/18%
514 as the nose length increase to 7.4m and 9.4m respectively. As a result, increasing the length of the
515 nose could reduce the magnitude and fluctuation of wake slipstream. However, this effect to reduce
516 the wake velocity is weakened in the tunnel.

517 **References**

1. Howe, M., Iida, M., Fukuda, T. & Maeda, T., 2000. Theoretical and experimental investigation of the compression wave generated by a train entering a tunnel with a flared portal. *Journal of Fluid Mechanics*, pp. 111-132.
2. Chen, G. et al., 2019. Dynamic analysis of the effect of nose length on train aerodynamic performance. *Journal of Wind Engineering and Industrial Aerodynamics*, 184(2019), pp. 198-208.
3. Bell, J. et al., 2014. Wind tunnel analysis of the slipstream and wake of a high-speed train. *Journal of Wind Engineering and Industrial Aerodynamics*, pp. 122-138.
4. Baker, C. J. et al., 2001. The slipstream and wake of a high-speed train. *Proceedings of the Institution of Mechanical Engineers, Part F: Journal of Rail and Rapid Transit*, 215(2), pp. 83-99.
5. Sterling, M., Baker, C., Jordan, S. & Johnson, T., 2008. A study of the slipstreams of high-speed passenger trains and freight trains. *Proceedings of the Institution of Mechanical Engineers, Part F: Journal of Rail and Rapid Transit*, 222(2), pp. 177-193.
6. Tian, H., 2019. Review of research on high-speed railway aerodynamics in China. *Transportation Safety and Environment*, 1(1), pp. 1-21.
7. Baker, C. et al., 2014a. Full-scale measurement and analysis of train slipstreams and wakes. Part 1: Ensemble averages. *Proceedings of the Institution of Mechanical Engineers, Part F: Journal of Rail and Rapid Transit*, 228(5), pp. 451-467.
8. Huang, S., Hemida, H. & Yang, M., 2016. Numerical calculation of the slipstream generated by a CRH2 high-speed train. *Proceedings of the Institution of Mechanical Engineers, Part F: Journal of Rail and Rapid Transit*, 230(1), pp. 103-116.
9. Hemida, H. & Baker, C., 2012. The Calculation of Train Slipstreams using Large-Eddy Simulation. *Journal of Rail and Rapid Transit*, 228(1), pp. 25-36.
10. Flynn, D., Hemida, H., Soper, D. & Baker, C., 2014. Detached-eddy simulation of the slipstream of an operational freight train. *Journal of Wind Engineering and Industrial Aerodynamics*, Volume 132, pp. 1-12.

11. Soper, D., Baker, C. & Sterling, M., 2014. Experimental investigation of the slipstream development around a container freight train using a moving model facility. *Journal of Wind Engineering and Industrial Aerodynamics*, Volume 135, pp. 105-117.
12. Bell, J. et al., 2016. Dynamics of trailing vortices in the wake of a generic high-speed train. *Journal of Fluids and Structures*, Volume 65, pp. 238-256.
13. Bell, J. et al., 2017. The effect of tail geometry on the slipstream and unsteady wake structure of high-speed trains. *Experimental Thermal and Fluid Science*, Volume 83, pp. 215-230.
14. Hemida, H., & Krajnović, S., 2010. LES study of the influence of the nose shape and yaw angles on flow structures around trains. *Journal of Wind Engineering and Industrial Aerodynamics*, 98(1), 34-46.
15. Mohebbi, M., & Rezvani, M. A., 2019. Analysis of the effects of lateral wind on a high speed train on a double routed railway track with porous shelters. *Journal of Wind Engineering and Industrial Aerodynamics*, 184, 116-127.
16. Rezvani, M. A., & Mohebbi, M., 2014. Numerical Calculations of Aerodynamic Performance an ATM Train at Crosswind Conditions. *Wind and Structures*, Vol. 18, No. 5, pp. 529-548.
17. Mohebbi, M., & Rezvani, M. A., 2018. The Impact of Air Fences Geometry on Air Flow around an ICE3 High Speed Train on a Double Line Railway Track with Exposure to Crosswinds. *JOURNAL OF APPLIED FLUID MECHANICS (JAFM)*, 11(3), 743-754.
18. Mohebbi, M., & Safaee, A. M., 2021. The optimum model determination of porous barriers in high-speed tracks. *Proceedings of the Institution of Mechanical Engineers, Part F: Journal of Rail and Rapid Transit*.
19. Mohebbi, M., & Rezvani, M. A., 2018. Two-dimensional analysis of the influence of windbreaks on airflow over a high-speed train under crosswind using lattice Boltzmann method. *Proceedings of the Institution of Mechanical Engineers, Part F: Journal of Rail and Rapid Transit*, 232(3), 863-872.
20. Mohebbi, M., & Rezvani, M. A., 2018. Multi objective optimization of aerodynamic design of high speed railway windbreaks using Lattice Boltzmann Method and wind tunnel test results. *International Journal of Rail Transportation*, 6(3), 183-201.
21. Suzuki, M., Ido, A., Sakuma, Y. & Kajiyama, H., 2008. Full-scale measurement and numerical simulation of flow around high-speed train in tunnel. *Journal of mechanical systems for transportation and logistics*, 1(3), pp. 281-292.
22. Fei, R. Z., Li, M. P., Wei, C. Y. & Wei, G. Y., 2014. Research of train wind characteristics in high-speed railway tunnel. *In Advanced Materials Research*, Volume 919, pp. 865-868.
23. Liu, T., Tian, H. & Liang, X., 2010. Aerodynamic effects caused by trains entering tunnels. *Journal of Transportation Engineering*, 136(9), pp. 846-853
24. Gilbert, T., Baker, C. & Quinn, A., 2013. Gusts caused by high-speed trains in confined spaces

- and tunnels. *Journal of wind engineering and industrial aerodynamics*, Volume 121, pp. 39-48.
25. Jiang, Z. et al., 2019. Numerical prediction of the slipstream caused by the trains with different marshalling forms entering a tunnel. *Journal of Wind Engineering and Industrial Aerodynamics*, Volume 189, pp. 276-288.
26. Li, W. & Liu, T., 2017. Three-dimensional Characteristics of the Slipstream Induced by a High-Speed Train Passing through a Tunnel. *DEStech Transactions on Engineering and Technology Research*, Volume icia.
27. Iliadis, P., Hemida, H. & Soper, D., 2019. Numerical simulations of the separated flow around a freight train passing through a tunnel using the sliding mesh technique. *Proceedings of the Institution of Mechanical Engineers, Part F: Journal of Rail and Rapid Transit*, 237(8), pp. 857-868.
28. Faramehr, S. & Hemida, H., 2016. Aerodynamics of Trains in Tunnels., in *Proceedings of the Third International Conference on Railway Technology: Research, Development and Maintenance*, Civil-Comp Press, p. Paper 36.
29. Wang, S. et al., 2017. The performance of different turbulence models (URANS, SAS and DES) for predicting high-speed train slipstream. *Journal of Wind Engineering and Industrial Aerodynamics*, Volume 165, pp. 46-57.
30. Khayrullina, A., Blocken, B., Janssen, W. & Straathof, J., 2015. CFD simulation of train aerodynamics: Train-induced wind conditions at an underground railroad passenger platform. *Journal of Wind Engineering and Industrial Aerodynamics*, Volume 139, pp. 100-110.
31. CEN, 2013. Railway Applications – Aerodynamics. Part 4: Requirements and Test Procedures for Aerodynamics on Open Track., In: *CEN EN*. s.l.:s.n., pp. 14067-4.
32. Niu, J., Wang, Y., Zhang, L. & Yuan, Y., 2018. Numerical analysis of aerodynamic characteristics of high-speed train. *International Journal of Heat and Mass Transfer*, 127(2018), pp. 188-199.
33. Hemida, H. & Krajnović, S., 2008. LES study of the influence of a train-nose shape on the flow structures under cross-wind conditions. *Journal of fluids engineering*, 130(9), pp. 1-12.
34. Li, X., Chen, G., Zhou, D. & Chen, Z., 2019. Impact of Different Nose Lengths on Flow-Field Structure around a High-Speed Train. *Applied Sciences*, 9(21), p. 4573.
35. Mohebbi, M., & Rezvani, M. A., 2021. 2D and 3D numerical and experimental analyses of the aerodynamic effects of air fences on a high-speed train. *Wind and Structures*, 32(6), 539-550.
36. Xia, C. et al., 2017. Effects of ground configurations on the slipstream and near wake of a high-speed train. *Journal of Wind Engineering and Industrial Aerodynamics*, Volume 168, pp. 177-189.
37. Liu, C, et al., 2017. Application of hybrid RANS/LES turbulence models in rotor-stator fluid machinery: a comparative study. *International Journal of Numerical Methods for Heat & Fluid Flow*, 27(12).
38. Shur, M., Spalart, P., Strelets, M. & Travin, A., 2008. A hybrid RANS-LES approach with

delayed-DES and wall-modelled LES capabilities. *International Journal of Heat and Fluid Flow*, 29(6), pp. 1638-1649.

39. Chen, X. & Zhang, X., 2013. High-Order Interface for Aeroacoustic Computation Using Overset Grid. *AIAA journal*, 51(2), pp. 519-523.

40. Wang, G. et al., 2014. An overset grid method for large eddy simulation of turbomachinery stages. *Journal of Computational Physics*, Volume 274, pp. 333-355.

41. Baker, C. et al., 2014b. Full-scale measurement and analysis of train slipstreams and wakes. Part 2 Gust analysis. *Proceedings of the Institution of Mechanical Engineers, Part F: Journal of Rail and Rapid Transit*, 228(5), pp. 468-480.

42. Baker, C., 2010. The flow around high speed trains. *Journal of Wind Engineering and Industrial Aerodynamics*, 6-7(277-298), p. 98.